RSC Advances

PAPER

View Article Online
View Journal | View Issue

Cite this: *RSC Adv.*, 2024, **14**, 1377

Research on the environmental stability performance of chromite ore processing residue solidified products†

Ming Xia, *[abc] Pengyue Su,[a] Hao Wang,[a] Huicheng Lu,[a] Haiyu Chen,[a] Shujie Zhao*[d] and Dongwei Li*[e]

Chromite ore processing residue (COPR) is a hazardous waste because of leachable chromium, especially Cr(VI). Therefore, ascorbic acid (AA) and blast furnace slag (BFS) have been used to detoxify and solidify COPR. On this basis, environmental stability experiments with high temperature and freeze–thaw cycles were carried out to explore the stability performance of a solidified body with 40% COPR. The environmental stability performance was analyzed through changes in edge length, mass loss, compressive strength development, and leaching concentration of Cr(VI). The result indicated that the high-temperature environment had much more effect on the solidified body than the freeze–thaw cycle environment in these four aspects: after being maintained at 900 °C for 2 h, the compressive strength of the solidified bodies reached its minimum value (35.76 MPa). However, in the freeze–thaw cycle experiments, the compressive strength of the solidified bodies consistently remained above 80 MPa, and the leaching of hexavalent chromium was below the limit (5 mg L^{-1}). In addition, X-ray diffraction (XRD) and Fourier transform infrared spectrometry (FTIR) analysis verified that COPR was effectively solidified through physical and chemical means. Moreover, high temperature changes the molecular structure of the solidified body, thus reducing the compressive strength and curing ability of the solidified body, while the freeze–thaw cycle experiment has little effect on it.

Received 7th October 2023
Accepted 19th December 2023

DOI: 10.1039/d3ra06820j

rsc.li/rsc-advances

1. Introduction

Chromite ore processing residue (COPR) is a kind of hazardous waste because of the existence of highly leachable and carcinogenic hexavalent chromium (Cr(VI)), which is generated during chromium salt production. While chromium salt is an important strategic resource which is widely used in electroplating, tanning, chemical reagents, wood preservatives, ceramics, dyes, and pigments.[1,2] On the one hand, inappropriate disposal of COPR occupies a large amount of land. On the other hand, the leaching of Cr(VI) from COPR pollutes farmland and water resources and ultimately threatens human life.[3,4] Additionally, the susceptibility of Cr(VI) causes some disorders such as skin allergies, erosive rhinitis, emphysema, bronchiectasis, and lung sclerosis in human beings.[1,5,6] Consequently, the appropriate disposal of COPR brooks no delay.

Technologies dealing with COPR could be divided into five main categories: (I) Solidification/stabilization (S/S) technology,[7–9] which means that the chromium in COPR is transformed into states and forms that are insoluble, migratory or less toxic by physical and chemical means using some materials such as ordinary Portland cement or alkali-activated cementitious material; (II) chemical reduction technology, including dry-detoxification (utilizing some reducing gases, such as CO) and wet-detoxification (reduction of Cr(VI) to Cr(III) in the liquid phase);[10–12] (III) microbial techniques,[13–15] *i.e.* the reduction of Cr(VI) in COPR by microorganisms; (IV) resource utilization methods,[16,17] in which COPR is used as an alternative material to produce certain products, transforming it into useful substances that promote the recycling of waste, such as sintered iron and glass colorants; (V) compound treatment technology,[18–20] which refers to using multiple technologies at the same time. S/S is usually considered to be the best available technique to treat solid hazardous wastes because of its convenience, economy, and high efficiency.[21] In particular, alkali-activated cementitious material is an excellent material used in the solidification of heavy metals because of lower CO_2 emission, energy conservation, higher compressive strength and good chemical corrosion resistance.[20,22]

[a]*School of Environmental and Chemical Engineering, Jiangsu Ocean University, Lianyungang, 222005, China. E-mail: xiaming@jou.edu.cn*

[b]*Jiangsu Institute of Marine Resources Development, Jiangsu Ocean University, Lianyungang, 222005, China*

[c]*Jiangsu Key Laboratory of Function Control Technology for Advanced Materials, Jiangsu Ocean University, Lianyungang, 222005, China*

[d]*School of Safety Science and Engineering, Anhui University of Science and Technology, Huainan, 232001, China. E-mail: zsj9506@163.com*

[e]*State Key Laboratory of Coal Mine Disaster Dynamics and Control, Chongqing University, Chongqing, 400044, China. E-mail: litonwei@cqu.edu.cn*

† Electronic supplementary information (ESI) available. See DOI: https://doi.org/10.1039/d3ra06820j

The solidification of chromite ore processing residue is based on environmental protection and resource utilization, and effectively curing harmful elements, reducing negative effects, and developing a harmless and low-emission curing process are the main development directions at this stage. New materials are being used to improve curing efficiency and quality, improve curing capacity while reducing carbon emissions, and to improve solid waste resource utilization.[23] Many researchers have been focusing on the immobilization of chromium in COPR.[7,9,20] Muhammad *et al.* 2020 (ref. 20) used composite-based geopolymer (BFS and metakaolin) and green tea synthesized nanoscale zerovalent iron (GT-NZVI) to solidify COPR, and they found that the compressive strength of the cured body with GT-NZVI particles was not greatly reduced, but the leaching toxicity was far below the safety limit (5 mg L^{-1}), indicating that COPR was effectively solidified in the composite-based geopolymer. Sun *et al.* 2014 (ref. 24) applied alkali-activated cementitious material (metakaolin) and sodium sulfate (Na_2SO_4) together to solidify COPR, and found that the leaching concentrations of Cr(VI) and total Cr were below 5 μg mL^{-1} and the compressive strength of the solidified body was over 40 MPa. Yu *et al.* 2021 (ref. 9) conducted solidification/stabilization of alkali-activated lead-zinc smelting slag (LZSS) and COPR, and found that the highest compressive strength of alkali-activated LZSS was 84.49 MPa, and the compressive strength was reduced to 1.42 MPa when the COPR content was 40%. However, the leaching concentrations of Zn and Cr in all cured bodies were well below the critical limits.

Generally, they just considered the leaching behaviors and compressive strength development of the COPR solidified body in a normal environment and ignored them under different environmental conditions. For one thing, the results of some research indicated that the solidified body can only be used for landfill,[20,22] which will cause a waste of resources. For another thing, some researchers claimed that the solidified body could be used for construction materials because of the higher compressive strength and lower leaching concentration of Cr(VI), neglecting application scenarios and uses. However, different application scenarios and uses will lead to huge changes in the environment where the solidified body is located. How to measure and evaluate the environmental stability of solidified bodies in these different scenarios is the focus of our research.

In the current study, ascorbic acid (AA) and blast furnace slag (BFS) are used to detoxify and solidify COPR. AA is an important biological reductant with a nontoxic nature found in humans and animals.[25,26] While BFS is an industrial by-product discharged from a blast furnace during the smelting of pig iron.[27,28] Moreover, the environmental stability performance of the COPR solidified body was studied to explore and assess its stability in different environments. The environmental stability study of a COPR solidified body refers to the environmental stability performance of the solidified body under the influence of single extreme environments, including the following two aspects: (I) a high-temperature environmental stability experiment; (II) a freeze–thaw environmental stability experiment. The experimental research provides an effective basis and reference for an expansion of the range of applications and locations of COPR products. Furthermore, technical analysis methods, such as XRD and FTIR analysis, were further used for characterization and to determine the solidification mechanism.

2. Materials and methods

2.1 Materials

The BFS used in this experiment was brought from a steel factory located in Chongqing Municipality. While COPR was fetched from the Chongqing Minfeng chemical company in Chongqing Municipality. The chemical reagents, *i.e.* water glass ($Na_2SiO_3 \cdot 3.3H_2O$), sodium hydroxide (NaOH), and AA ($C_6H_8O_6$), used in this experiment were of analytical grade. Deionized water was used throughout the experiments. Based on the particle size distribution analysis depicted in Fig. S1† for COPR and the SEM images presented in Fig. S2,† it was evident that the majority of COPR particles fell within the range of 10 to 100 μm, showcasing an average particle size of 68.79 μm. These particles exhibited a small and irregular shape. At the same time, the SEM image of BFS displayed in Fig. S3† revealed that the BFS particles were generally small, measuring less than 100 μm in size, and exhibited considerable variation in size.

The chemical compositions of BFS and COPR were determined by X-ray fluorescence (XRF) using the powder pressing method, and are shown in Table 1. The main chemical components of BFS were CaO, SiO_2, and Al_2O_3 which constituted up to 86.6% of the material. In addition, 91.5% of COPR was composed of Fe_2O_3, Al_2O_3, Cr_2O_3, and MgO.

2.2 Methods

2.2.1 Preparation of the COPR solidified body. According to our previous experimental results, the optimal combination level was selected to prepare the solidified body. Accordingly, the modulus of water glass was 1.6, the liquid–solid ratio was 0.24, and the amount of AA was 0.7%, and the chromium slag content was 10–50%. Prior to utilization, an alkaline solution was prepared by adjusting the modulus of the water glass with NaOH for the initial 10 hour period. BFS and COPR were mixed (2 min) and then mixed with the alkaline solution until a dense

Table 1 The composition of COPR and BFS

Composition	COPR (wt%)	BFS (wt%)
Fe_2O_3	41.91	0.60
Al_2O_3	26.10	14.93
Cr_2O_3	13.35	—
MgO	10.16	7.50
Na_2O	3.39	0.22
SiO_2	2.60	35.62
TiO_2	1.31	1.28
V_2O_5	0.34	—
CaO	0.23	36.31
NiO	0.17	—
ZnO	0.14	—
SO_3	0.14	2.29
MnO	—	0.69
K_2O	—	0.39
Other	0.16	0.17

paste was achieved (5 min). Afterward, the dense paste was poured into 20 mm × 20 mm × 20 mm cubic molds and then vibrated for approximately 2 min to remove air bubbles. The samples were demolded after curing at 25 °C for 24 h and kept at ambient temperature for the rest of the time (27 d). Additionally, samples each with three replicates were prepared according to the layout given in Table 2.

2.2.2 High-temperature environmental stability. After 28 d of curing, the samples were put into a muffle furnace (XH5L-16, Xinhan, China) to explore their stability in a high-temperature environment. There were was a total of 12 groups of experiments, including 4 different temperatures (300 °C, 600 °C, 900 °C, and 1200 °C) and 3 different time periods (1 h, 2 h, and 3 h), which are shown in Table 3. After that, the leaching concentration of Cr(VI), and the compressive strength, weight, and edge length of these samples were tested and recorded.

2.2.3 Freeze–thaw environment stability. In this part, different numbers of freeze–thaw cycles (5, 10, 25, 50, 75, 100) were selected to investigate the stability of the COPR solidified body in a cyclic freeze–thaw environment.

In order to simulate the use of the solidified body in cold conditions, multiple freeze–thaw experiments help to determine the durability and stability of the solidified body, especially to simulate the exposure to cold environments when used as building materials. The advantage of designing 100 freeze–thaw experiments is that the performance changes of the solidified body can be observed during the freeze–thaw cycle, simulating the real conditions of use, and helping to predict the performance in actual use and the improvement of the conditions of the solidified body in later stages. The specific steps are as follows.

(1) After 24 d of curing time, the samples were immersed in deionized water (20 ± 2 °C) for 4 d, and then freeze–thaw experiments were carried out. The surface moisture of the samples was removed with a damp cloth, and the edge length and weight of the samples were measured.

(2) The above-mentioned specimens were placed on the test stand to ensure that the contact area was less than 80 mm^2 (1/5 bottom area), the gap between the test stand and the inner wall of the box was more than 20 mm, and the distance between the specimens on the test stand was over 10 mm.

(3) When the temperature in the box dropped to −18 °C, the freeze–thaw experiment began. In addition, the time from the completion of loading samples to the temperature in the box dropping to −18 °C was controlled from 1.5 to 2 h. The temperature in the box was maintained between −20 °C and −18 °C, and the freezing time in a single freeze–thaw cycle was more than 4 h.

Table 2 The composition of the COPR solidified body

Name	BFS/g	COPR/g	Solid alkali/g	AA/g
BCA10	81	10	9	0.07
BCA20	72	20	8	0.14
BCA30	63	30	7	0.21
BCA40	54	40	6	0.28
BCA50	45	50	5	0.35

Table 3 High-temperature stability experiment schedule

Serial number	Temperature (°C)	Stay time (h)
1	300	1
2	300	2
3	300	3
4	600	1
5	600	2
6	600	3
7	900	1
8	900	2
9	900	3
10	1200	1
11	1200	2
12	1200	3

(4) After freezing, the deionized water (the water temperature was 18 °C to 20 °C) was added, and the addition time was less than 10 minutes. The water temperature was over 10 °C within 30 minutes and then maintained at 18 °C to 20 °C after 30 minutes. The thawing time in a single freeze–thaw cycle was more than 4 hours.

(5) After reaching the corresponding freeze–thaw times, the mass loss of the solidified body was weighed and calculated; the compressive strength loss of the solidified body was measured and calculated; the leaching concentration of Cr(VI) in the solidified body was measured, and the influence of the freeze–thaw environment was explored.

2.2.4 Characterization analysis. The average compressive strengths of three replicates after 28 d were determined with a universal testing machine (AGN-250, Shimadzu, Japan) which was operated at a speed of 1 mm min^{-1}. The sulfuric and nitric acid method as per Chinese Environmental Protection Standard HJ/T 299-2007 (ref. 29) was used to leach Cr(VI) from COPR and the solidified body. In addition, the Cr(VI) concentrations were determined with the 1,5-diphenylcarbohydrazide spectrophotometric method (GB/T 15555. 4-1995, 1995).[30] According to this method, a crushed sample (<9.5 mm) was added to the extract and shaken at a rate of 30 rpm for 18 hours. The extraction solution was a mixture of concentrated sulfuric acid and nitric acid according to mass ratio 2 : 1, dissolved in ionized water, and the pH value was maintained at 3.20 ± 0.05 in the extraction solution. The solid–liquid ratio was 1 : 10.

The XRD was examined by using an X-ray diffractometer (PANalytical X'Pert Powder, Holland) with CuKα radiation, and the specimens were step-scanned as random powder mounts from 5° to 90° with steps of 0.026°. While FTIR analysis was performed using a Nicolet-IS50 (Thermo Fisher Scientific Inc, USA) FTIR spectrometer in the range of 4000–400 cm^{-1}.

3. Results and discussions

3.1 Solidification/stabilization (S/S) of COPR

3.1.1 The compressive strength of solidified bodies containing COPR. On the whole, the compressive strength of the solidified samples (28 d) decreased with the increment of COPR percentage (10–50%), as can be seen in Fig. 1. Specifically, the

compressive strength of the solidified body was higher than 100 MPa when the addition of COPR was less than 30%. When the COPR content increased to 40%, the compressive strength was slightly lower than 90 MPa (89.83 MPa). With the COPR continuing to increase (50% COPR), the strength of the solidified body reduced to 54.67 MPa, which was still high enough to be satisfactory for construction purpose and landfill disposal. According to Table 1, it was found that Si and Ca in COPR were extremely deficient. In addition, the XRD pattern of COPR in Fig. S4† showed that the crystallinity of COPR was high and provided no active reactants in the later S/S process, which both harmed compressive strength development.

3.1.2 The leaching concentration of Cr(VI). The relationship between the leaching concentration of Cr(VI) in COPR solidified bodies and COPR addition is shown in Fig. 2. While the leaching concentration of Cr(VI) gradually increased with the increment in COPR (0.16–2.56 μg mL^{-1}), which was far lower than the limit in GB 5085.3-2007 (ref. 31) (shown in Table 4). Moreover, there was a high probability that chromium in these solidified samples was immobilized by physical and chemical means.[21,32] The Cr(VI) leaching concentrations in solidified samples with 20% and 30% COPR addition were 0.44 μg mL^{-1} and 0.97 μg mL^{-1} (0.44 μg mL^{-1} < 0.5 μg mL^{-1} < 0.97 μg mL^{-1}), respectively. According to the 'Environmental Protection Technical Specifications for Pollution Treatment of the Chromium Residue' (HJ/T 301-2007), the Cr(VI) leaching concentration in the solidified bodies with no more than 20% addition of COPR meets the limit for roadbed material and concrete aggregate (Table 4). When the content of COPR in the solidified sample was 50%, the leaching concentration of Cr(VI) was 2.56 μg mL^{-1} (<3 μg mL^{-1}), which indicated that the leaching concentration of Cr(VI) in the solidified body (≤50% COPR) meets the requirements for common industry solid waste landfill (Table 4).

3.2 High-temperature environmental stability of COPR solidified bodies

3.2.1 Edge length loss and mass loss of solidified samples at high temperature. The edge length loss ($L_{edge,i}$, %) was calculated according to eqn (1). $L_{edge,i}$ refers to the edge length loss of the solidified body in group i ($1 \leq i \leq 12$, $I \in N$). $EL_{before(ij)}$ and $EL_{after(ij)}$ ($1 \leq j \leq 3, j \in N$) are the average edge length (mm) of solidified bodies (BCA40) in group i before and after high-temperature calcination, respectively.

$$L_{edge,i} = \left[\sum_{j=1}^{3} \frac{EL_{before(ij)} - EL_{after(ij)}}{EL_{before}(ij)}\right] \Big/ 3 \times 100\% \quad (1)$$

In order to quantify the mass loss of the solidified specimens (BCA40) at high temperature, the mass loss rate of each group of specimens was calculated according to eqn (2).

$$L_{weight,i} = \left[\sum_{j=1}^{3} \frac{W_{before(ij)} - W_{after(ij)}}{W_{before}(ij)}\right] \Big/ 3 \times 100\% \quad (2)$$

$L_{weight,i}$ refers to the mass loss of the solidified body in group i. $W_{before(ij)}$ and $W_{after(ij)}$ are the average weight (g) of the solidified body in group i before and after high-temperature calcination, respectively. Additionally, i and j are the same as in eqn (1).

The calculation results of edge length loss and mass loss in each group of solidified bodies are shown in Fig. 3. It can be seen that the edge length loss increased gradually with an increase in calcination temperature (the abscissa serial number 1–12 in the graph is consistent with Table 3). In particular, when

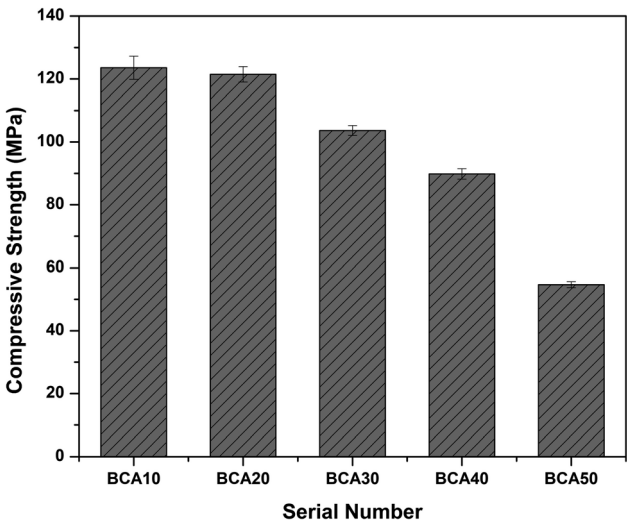

Fig. 1 The compressive strength of solidified bodies containing COPR.

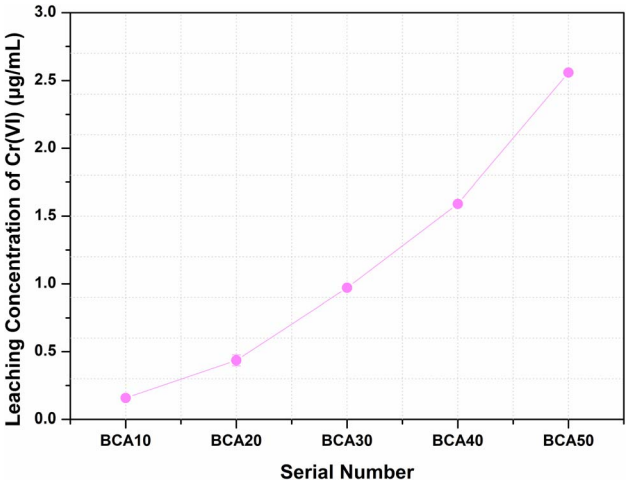

Fig. 2 The leaching concentration of Cr(VI) from solidified samples.

Table 4 The relevant limits of Cr(VI)

Related instructions	Standards	Cr(VI)/ (μg mL^{-1})
Hazardous waste identification	GB 5085.3-2007	5
Common industry solid waste landfill	HJ/T 301-2007	3
Roadbed material and concrete aggregate	HJ/T 301-2007	0.5

the temperature was less than 900 °C, the edge length loss increased by almost double with the increase in temperature, but the edge length loss rate was kept within 5%. When the calcination temperature was further raised to 1200 °C, the growth rate of the edge length loss rate decreased, but the rate of edge length loss of the solidified body reached a maximum of 7.28% ($L_{edge,12}$) after being held for 3 hours at this temperature.

According to Fig. 3, the mass loss rate of these specimens was concentrated in the range 15.5–18.5%; except for numbers 3, 9, 11 and 12, and the other 8 groups were concentrated in the range of 17.0–18.0%. In addition, the mass loss presented an increasing trend with rising temperature. The water evaporation caused by high temperature was the main reason for the mass loss.

3.2.2 The compressive strength development of solidified samples at high temperature. The variation in the compressive strength of the COPR solidified body (BCA40) with calcination temperature and heat preservation time can be seen in Fig. 4. From the point of view of the temperature dimension, the compressive strength of BCA40 decreased with an increase in calcination temperature up to 1200 °C (without the inclusion of 1200 °C): the compressive strength of the control group without high-temperature treatment was 89.83 MPa, which was reduced to 62.52 MPa for 3 h at 300 °C, to 42.92 MPa for 1 h at 600 °C and to 35.76 MPa for 2 h at 900 °C. For the dimension of heat preservation time, the rule for change in compressive strength was not the same: 1 h and 2 h heat preservation time at these temperatures (*i.e.* 300, 900, and 1200 °C) had little effect on strength development, and the strength was basically the same, but when the heat preservation time reached 3 h, the strength decreased or increased. While the difference in compressive strength between the samples with 2 h and 3 h heat preservation decreased gradually with an increase in temperature, and tended to be stable when the temperature reached 1200 °C.

3.2.3 Leaching test. The leaching concentration of Cr(VI) in a solidified body (BCA40) varied with temperature (300, 600, 900, and 1200 °C) and holding time (1, 2, and 3 h), as shown in Fig. 5. According to this figure, the leaching concentration of Cr(VI) showed an upward trend with increasing temperature

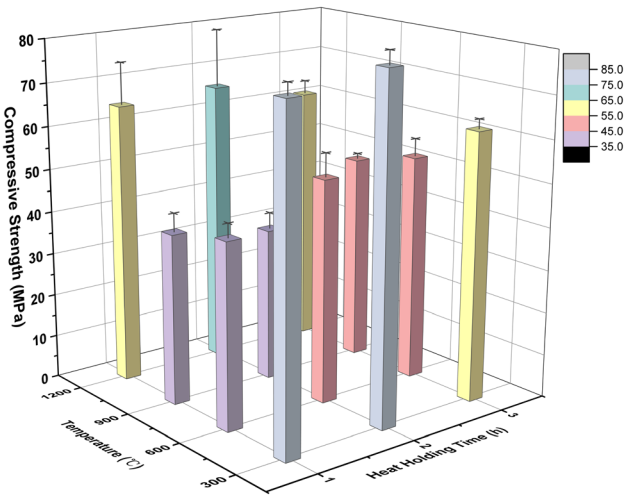

Fig. 4 The compressive strength of BCA40 varies with different temperatures and times.

(≤900 °C), reaching its maximum value (82.95 μg mL^{-1}) after being held for 1 h at 900 °C. However, when the temperature continued to rise to 1200 °C, the leaching concentration of Cr(VI) in the solidified body decreased sharply and remained at 1.11–1.26 μg mL^{-1}, which was below that in the control group (1.59 μg mL^{-1}). From the perspective of holding time, the Cr(VI) leaching concentration of the other three groups (300, 600, and 1200 °C) was minimally affected by the holding time and remained basically same except for the group at 900 °C, which showed a significant downward trend.

3.3 Freeze–thaw environment stability of COPR solidified bodies

3.3.1 Edge length loss and mass loss of solidified samples under the action of the freeze–thaw cycle. The relevant results can be seen in Fig. 6. Eqn (1) was used to calculate the loss rate of edge length, but the range of i changed to $1 \leq i \leq 6$ ($i \in$ N).

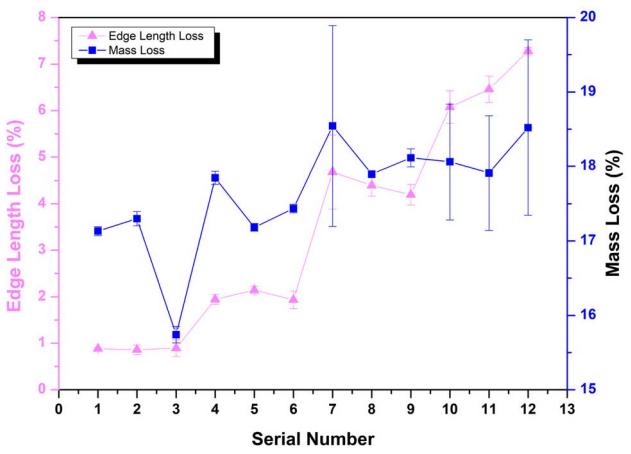

Fig. 3 The edge length loss and mass loss of BCA40 at high temperature.

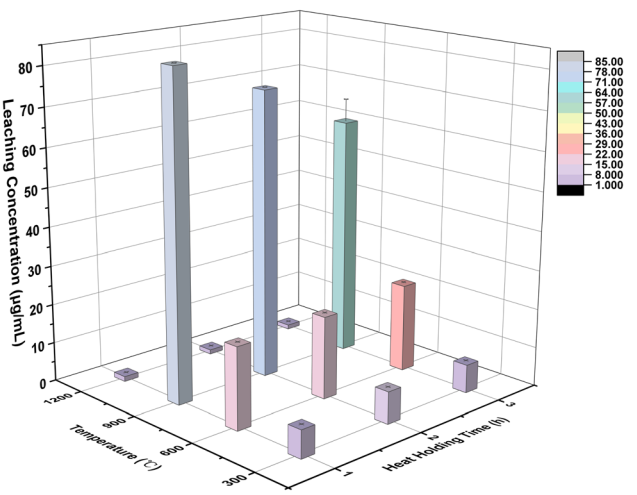

Fig. 5 The leaching concentration of Cr(VI) in BCA40 varies with different temperatures and times.

The rate of weight loss of the solidified bodies under different freeze–thaw cycles was calculated according to eqn (2).

The range of edge length fluctuation was very small at different freeze–thaw times. Moreover, the edge length loss rates of each group were all less than 0.5%. It can be seen that the freeze–thaw cycle effect has little influence on the change in edge length of solidified bodies, which could be neglected. In other words, the results indicated that there was no adverse effect on the appearance and volume of the solidified bodies under freeze–thaw cycles.

It can also be seen from Fig. 6 that the weight loss rates of the solidified bodies under freeze–thaw cycle conditions were at a low level, concentrated in the range 0.7–0.95%, and were greatly reduced when compared with those in the high-temperature environment (Fig. 3). Additionally, as the number of freeze–thaw cycles increased, the weight loss rate showed an increasing trend and reached a maximum value of 0.92% when the number of freeze–thaw cycles was 100.

3.3.2 The compressive strength development of solidified samples under the action of the freeze–thaw cycle. The compressive strength of the solidified bodies under different freeze–thaw cycles and the corresponding strength of the control groups can be seen in Fig. 7. According to Fig. 7, the compressive strength of all batches of solidified bodies remained above 80 MPa after different numbers of freeze–thaw cycles (5, 10, 25, 50, 75 and 100). Compared with the solidified body with 5 freeze–thaw cycles, the strength of the samples with 10 freeze–thaw cycles decreased slightly; after that, with an increase in freeze–thaw cycles, the strength of the solidified bodies obviously increased and tended to be stable. The compressive strength of the solidified specimens in the control group reached a maximum value (99.21 MPa) after 10 freeze–thaw cycles, and a minimum value (86.91 MPa) after 50 freeze–thaw cycles. Moreover, the compressive strength of the solidified bodies after the other numbers of cycles did not change significantly (<4%).

In addition, the compressive strength loss rate (L_{cs}, %) was calculated with eqn (3), as shown in Fig. 7. In eqn (3), P_n denotes the average compressive strength of the solidified bodies with n freeze–thaw cycles and P_{cn} denotes the average compressive strength of the corresponding control group.

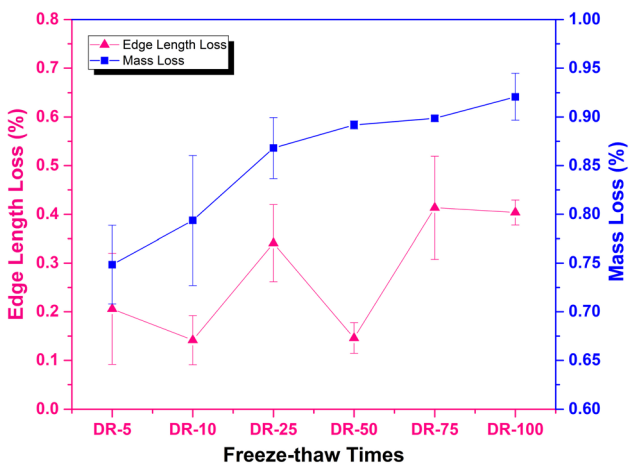

Fig. 6 The edge length loss and mass loss of BCA40 vary with different freeze–thaw times.

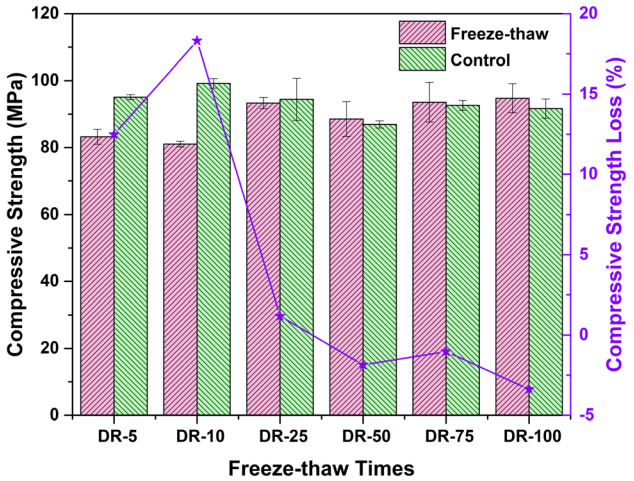

Fig. 7 The compressive strength of BCA40 varying with freeze–thaw times.

$$L_{cs} = \frac{P_{cn} - P_n}{P_{cn}} \times 100\% \quad (3)$$

It can be seen from Fig. 7 that the compressive strength loss was over 0 when the number of freeze–thaw cycles was less than 25 (including 25), which indicated that the freeze–thaw action had an adverse effect on the compressive strength of the solidified bodies, resulting in a decrease in compressive strength. In particular, when the number of freeze–thaw cycles was 10, the peak was reached (18.31%). While this situation was somewhat different when the number of freeze–thaw cycles exceeded 25. The trend of strength loss rate was relatively stable, and the strength loss rates were all below 0, suggesting that the compressive strength of "the freeze–thaw group" increased compared with the control group, and reached an extreme value of −3.38% after 100 freeze–thaw cycles.

3.3.3 Leaching test. The leaching concentration of Cr(VI) in solidified bodies after different numbers of freeze–thaw cycles (5, 10, 25, 50, 75, and 100) can be seen in Fig. 8. The figure indicates that the freeze–thaw environment has little influence on the release of Cr(VI) in the solidified samples. The leaching concentration of Cr(VI) in the solidified bodies under different cycles was somewhat higher than that in the control group, reaching a maximum of 3.26 mg L^{-1} when the number of freeze–thaw cycles was 75.

3.4 XRD analysis

The XRD patterns of solidified bodies, *i.e.* BCA40, T900-1 (BCA40 at 900 °C for 1 h), and T1200-3 (BCA40 at 1200 °C for 3 h) are illustrated in Fig. 9.

By and large, the XRD pattern of BCA40 was pretty different from that of T900-1 or T1200-3. For BCA40, magnesiochromite, ferroan (PDF#:09-0353), iron silicate (PDF#:80-1625), and magnesium aluminium iron oxide (PDF#:71-1235) were the

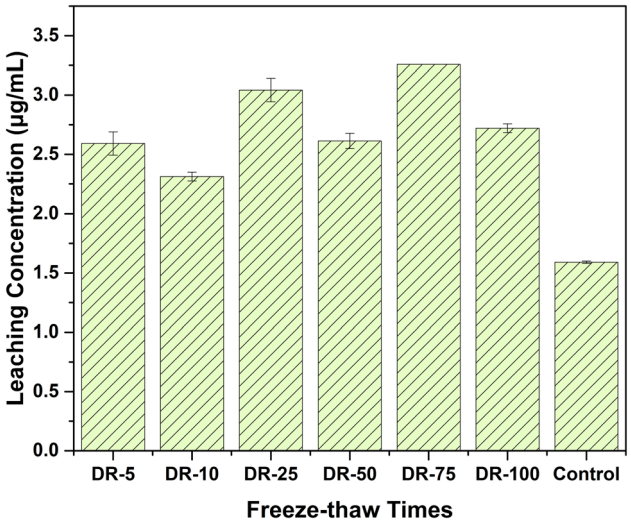

Fig. 8 The leaching concentration of Cr(VI) in BCA40 varying with freeze–thaw times.

principal phases. Both T900-1 and T1200-3 had identical phases (magnesiochromite, ferroan) to that of BCA40, but the peak intensities were reduced after high-temperature treatment. Additionally, new phases, *i.e.* gehlenite (PDF#: 77-1147) and aluminum chromium iron (PDF#: 42-1486), appeared in the T900-1 sample. While iron silicate disappeared and gehlenite was generated in T1200-3. This phenomenon could be attributed to the involvement of heavy metal chromium, released due to high-temperature damage, which further engages in the formation of a new phase. Consequently, this leads to a decrease in the leaching of hexavalent chromium at T1200-3.

The solidified bodies after 10 and 75 freeze–thaw cycles (DR10 and DR75) were chosen as representative samples for XRD analysis in Fig. 10. Generally speaking, the XRD patterns of DR10, DR75, and BCA40 were similar. In other words, magnesiochromite, ferroan and iron silicate were the main phases, which could explain why the results for compressive strength (Fig. 7) and Cr(VI) leaching concentration (Fig. 8) changed little between DR10 (75) and BCA40.

3.5 FTIR analysis

The FTIR spectra of the solidified bodies (BCA40, T900-1, T1200-3, DR10, and DR75) are presented in Fig. 11 (the FTIR spectra of COPR can be seen in Fig. S5†). The stretching bands in the range 3000 cm^{-1}–3500 cm^{-1} of samples BCA40, DR10, and DR75 were due to OH vibration,[21,33,34] which were formed due to the adsorption of water either on the surface or in structural cavities of the cementitious binder. However, for samples T900-1 and T1200-3, the OH stretching vibration disappeared due to the high temperature. Additionally, the 430 cm^{-1} band was attributed to Si–O–Si bending vibration.[35] The asymmetric stretching vibration peaks between 900 cm^{-1} and 1000 cm^{-1} corresponded to Si–O and Al–O bonds. These findings were also supported by some results in the literature (Muhamad *et al.*, 2019; San Cristobal *et al.*, 2010; Santa *et al.*, 2013).[20,36,37] It is noteworthy that the asymmetric stretching band of Si–O–Al (Si) in BCA40 at a wavenumber of 953.70 cm^{-1} shifted towards a smaller wavenumber, *i.e.*, T900-1 at 907.11 cm^{-1} and T1200-3 at 907.61 cm^{-1}, which was related to the degree of polymerization of the Si–O bonds. In addition, the 'high-temperature samples' have a new absorption band in the wavenumber range 600–620 cm^{-1}, corresponding to the bending vibration of Si–O–Al, which was related to the new phase gehlenite and aluminum chromium iron found in the XRD patterns.

Furthermore, the asymmetric stretching band at approximately 1420 cm^{-1} was due to carbonates, which resulted from the

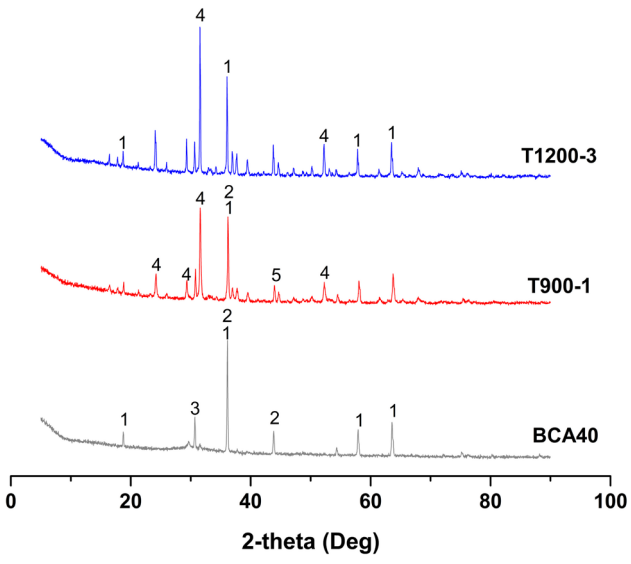

Fig. 9 The XRD patterns of solidified bodies in a high-temperature environment. (1) magnesiochromite, ferroan ($(Mg, Fe)(Cr, Al)_2O_4$), (2) iron silicate ($Fe_2(SiO_4)$), (3) magnesium aluminium iron oxide ($MgAl_{1.8}Fe_{1.2}O_4$), (4) gehlenite ($Ca_2Al(AlSi)O_7$) and (5) aluminum chromium iron ($AlCrFeO_4$).

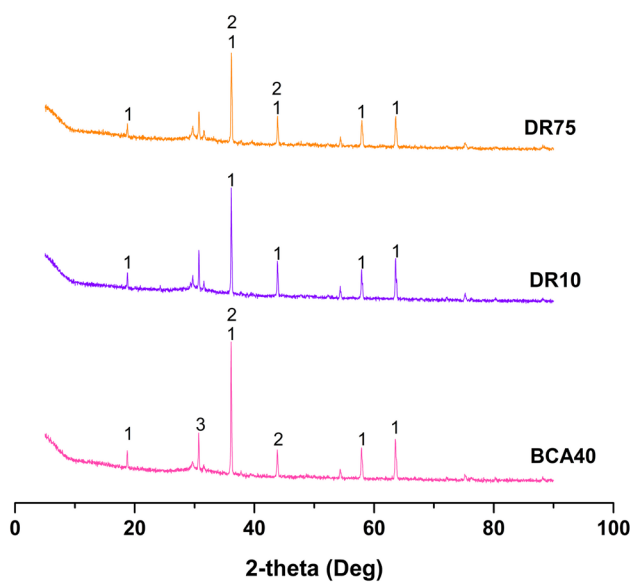

Fig. 10 The XRD patterns of solidified bodies in the freeze–thaw environment. (1) magnesiochromite, ferroan ($(Mg, Fe)(Cr, Al)_2O_4$), (2) iron silicate ($Fe_2(SiO_4)$), (3) magnesium aluminium iron oxide ($MgAl_{1.8}Fe_{1.2}O_4$).

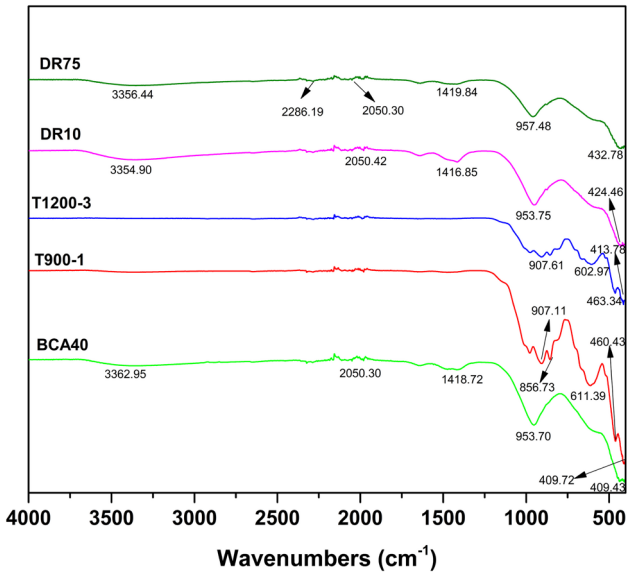

Fig. 11 The FTIR spectra of solidified bodies.

reaction of alkali metal hydroxide with atmospheric CO_2.[36,38,39] While the asymmetric stretching band of carbonates in the wavenumber range from 1400 to 1500 cm^{-1} disappeared in T900-1 and T1200-3, which could be caused by the thermal decomposition of carbonates. The reaction equations related to carbonates can be seen in eqn (4)–(6). The evaporation of water and the generation of CO_2 gas can lead to the formation of pores and cracks inside and on the surface of the solidified body, which in turn affected the mechanical properties of the solidified body and led to loss of compressive strength. The low-temperature state effectively prevented the loss of water within the solidified body, slowed down the alteration of molecular structure in the material, and aided in maintaining the original performance and compressive strength of the solidified body.

$$CaCO_3 \xrightarrow{\Delta} CaO + CO_2 \quad (4)$$

the thermodynamic values (delta G) of eqn (4) was as follows.

$$\Delta_r G_m^\theta = \sum V_B \Delta_f G_m^\theta(B) \quad (5)$$

For eqn (4), $\Delta_r G_m^\theta = (-604.03 \times 1) + (-394.36 \times 1) - (-1128.79 \times 1) = 130.4$ kJ (298.15 K, 100 kPa)

$$\Delta G = \Delta H - T\Delta S \text{ (100 kPa)} \quad (6)$$

$\Delta H = (-635.09) + (-393.51) - (-1206.92) = 178.32$ kJ mol^{-1}, $\Delta S = 39.75 + 213.74 - 92.9 = 160.59$ J mol^{-1} K^{-1}, $T = 1173.15$ K (900 °C), $\Delta G = -10.08$ kJ mol^{-1}, $T = 1473.15$ K (1200 °C), $\Delta G = -52.25$ kJ mol^{-1}.

4. Conclusions

The detoxification and immobilization of COPR by AA and BFS were studied experimentally. The real properties of the cured body were simulated through a high-temperature experiments and freeze–thaw cycle experiments, and the environmental stability performance of the solidified body was analyzed through four aspects: (a) edge length loss; (b) mass loss; (c). compressive strength development and (d) leaching concentration of Cr(VI). This provides a basis and reference for the application range and application sites of curing products.

(1) In the high-temperature environment, the highest edge loss and weight loss were 7.28% and 18.54% respectively. However, the free–thaw cycle environment had hardly any impact on the edge loss (<0.50%) or weight loss (≤1.00%). The lowest compressive strengths were 35.76 MPa and 81.04 MPa for high-temperature and freeze–thaw cycle environments, and the solidified body still had good mechanical properties. For the Cr(VI) leaching concentration, all the groups in the freeze–thaw cycle environment were slightly higher than in the control group (3.37 μg mL^{-1}), but below the safety threshold (5 μg mL^{-1}). But the high-temperature experiment found that the concentration of Cr(VI) rose from 1.11 μg mL^{-1} (1200 °C) to 82.95 μg mL^{-1} (900 °C). The stability of immobilization had deteriorated. Overall, the solidified body shows great freeze–thaw resistance but poor high-temperature stability.

(2) XRD and FTIR analyses indicated that molecular structural changes occurred in the solidified bodies under high-temperature conditions, leading to the evaporation of internal moisture and the generation of CO_2, resulting in decreased compressive strength and solidification performance. However, the influence of low temperatures on the structure and solidification performance of the solidified bodies was minimal. This demonstrated that the solidified products exhibited better mechanical and solidification performance in low-temperature environments. Therefore, the later-stage application of the products could be concentrated in low-temperature environments.

Conflicts of interest

There are no conflicts of interest to declare.

Acknowledgements

This study was supported by the Natural Science Foundation of Jiangsu Province (Grant No. BK20210926), National Natural Science Foundation of China (No. 52304196) and Jiangsu Ocean University Talent Introduction Start-up Fund (No. KQ21007). It was also funded by Innovation and Entrepreneurship Training Program for College Students (SY202111641637017, SZ202111641637004) and Postgraduate Research and Practice Innovation Program of Jiangsu Ocean University (KYCX2023-15). Supported by Open-end Funds of Jiangsu Key Laboratory of Function Control Technology for Advanced Materials, Jiangsu Ocean University (JSKLFCTAM202006) and Open-end Funds of Jiangsu Institute of Marine Resources Development (JSIMR202020).

References

1 X. Huang, Research on solidification/stabilization of chromite ore processing residue using composite materials

based geopolymer and its enhanced techology, PhD thesis, Chongqing University, 2018.
2 Y. Y. Wang, Z. H. Yang, L. Y. Chai and K. Zhao, *J. Hazard. Mater.*, 2009, **169**, 1173–1178.
3 Y. Y. Li, J. L. Liang, Z. H. Yang, H. Wang and Y. S. Liu, *Sci. Total Environ.*, 2019, **658**, 315–323.
4 Y. X. Liu, H. Q. Zhu, M. L. Zhang, R. Y. Chen, X. Chen, X. Zheng and Y. C. Jin, *J. Membr. Sci.*, 2018, **566**, 190–196.
5 E. Erdem, R. Donat, K. Esen and T. Tunc, *Ceram.-Silik.*, 2011, **55**, 85–93.
6 Y. Y. Li, A. B. Cundy, J. X. Feng, H. Fu, X. J. Wang and Y. S. Liu, *J. Environ. Manage.*, 2017, **192**, 100–106.
7 K. S. B. Kameswari, V. Pedaballe, L. M. Narasimman and C. Kalyanaraman, *Environ. Prog. Sustainable*, 2015, **34**, 674–680.
8 X. Huang, T. Huang, S. Li, F. Muhammad, G. J. Xu, Z. Q. Zhao, L. Yu, Y. J. Yan, D. W. Li and B. Jiao, *Ceram. Int.*, 2016, **42**, 9538–9549.
9 L. Yu, L. Fang, P. P. Zhang, S. J. Zhao, B. Q. Jiao and D. W. Li, *Int. J. Environ. Res. Public Health*, 2021, **18**, 9960.
10 T. G. Wang, M. L. He and Q. Pan, *J. Hazard. Mater.*, 2007, **149**, 440–444.
11 Y. Wang, J. Mao, X. G. Meng, L. Yu, D. H. Deng and X. H. Bao, *Chem. Rev.*, 2019, **119**, 1806–1854.
12 D. L. Zhang, M. Y. Zhang, C. H. Zhang, Y. J. Sun, X. Sun and X. Z. Yuan, *Environ. Sci. Technol.*, 2016, **50**, 3111–3118.
13 C. Y. Lai, L. Zhong, Y. Zhang, J. X. Chen, L. L. Wen, L. D. Shi, Y. P. Sun, F. Ma, B. E. Rittmann, C. Zhou, Y. N. Tang, P. Zheng and H. P. Zhao, *Environ. Sci. Technol.*, 2016, **50**, 5832–5839.
14 G. J. Xu, Study on the stabilization mechanism of microbial detoxication and encapsulation of chromium slag, PhD thesis, Chongqing University, 2017.
15 M. J. He, F. H. Wu, G. F. Qu and X. X. Liu, *Environ. Res.*, 2023, **238**, 117149.
16 J. N. Wu, C. L. Li and F. Yang, *J. Cleaner Prod.*, 2015, **95**, 156–162.
17 P. P. Zhan, L. H. Zeng, S. H. Zhang, C. W. Li and D. W. Li, *Environ. Sci. Pollut. Res.*, 2023, **30**, 29392–29406.
18 X. Huang, F. Muhammad, L. Yu, B. Q. Jiao, Y. Shiau and D. W. Li, *Ceram. Int.*, 2018, **44**, 3454–3463.
19 J. Li, Z. L. Chen, J. M. Shen, B. Y. Wang and L. T. Fan, *Chemosphere*, 2015, **134**, 159–165.
20 F. Muhammad, M. Xia, S. Li, X. Yu, Y. H. Mao, F. Muhammad, X. Huang, B. Q. Jiao, L. Yu and D. W. Li, *J. Cleaner Prod.*, 2019, **234**, 381–391.
21 M. Xia, F. Muhammad, L. H. Zeng, S. Li, X. Huang, B. Q. Jiao, Y. Shiau and D. W. Li, *J. Cleaner Prod.*, 2019, **209**, 1206–1215.
22 X. Huang, R. L. Zhuang, F. Muhammad, L. Yu, Y. C. Shiau and D. W. Li, *Chemosphere*, 2017, **168**, 300–308.
23 B. B. Sun, G. Ye and G. D. Schutter, *Constr. Build. Mater.*, 2022, **326**, 126843.
24 T. Sun, J. Y. Chen, X. R. Lei and C. Y. Zhou, *J. Environ. Chem. Eng.*, 2014, **2**(1), 304–309.
25 G. Afolaranmi and M. Grant, *Toxicology*, 2011, **290**, 120.
26 T. J. Lin, Y. L. Huang, J. S. Chang, K. T. Liu, M. C. Yen, F. W. Chen, Y. L. Shih, J. C. Jao, P. C. Huang and I. J. Yeh, *J. Trace Elem. Med. Biol.*, 2018, **48**, 1–7.
27 A. B. Hizon-Fradejas, Y. Nakano, S. Nakai, W. Nishijima and M. Okada, *J. Hazard. Mater.*, 2009, **166**, 1560–1566.
28 H. M. Khater, *Adv. Cem. Res.*, 2014, **26**, 1–9.
29 CN-HJ, *Solid Waste-Extraction Procedure for Leaching Toxicity-Sulphuric Acid and Nitric Acid Method (HJ/T 299-2007)*, 2007.
30 CN-GB, *Solid Waste-Determination of Chromium(vi)-1,5-Diphenylcarbohydrazide Spectrophotometric Method (GB/T 15555. 4-1995)*, 1995.
31 CN-GB, *Identification Standards for Hazardous Wastes-Identification for Extraction Toxicity (GB 5085.3-2007)*, 2007.
32 F. Muhammad, X. Huang, S. Li, M. Xia, M. L. Zhang, Q. Liu, M. A. S. Hassan, B. Q. Jiao, L. Yu and D. W. Li, *J. Cleaner Prod.*, 2018, **188**, 807–815.
33 C. Y. Hea and H. Kamarudin, *Constr. Build. Mater.*, 2012, **35**, 912–922.
34 R. K. Liew, W. L. Nam, M. Y. Chong, X. Y. Phang, M. H. Su, P. N. Y. Yek, N. L. Ma, C. K. Cheng, C. T. Chong and S. S. La, *Process Saf. Environ.*, 2018, **115**, 57–69.
35 W. K. W. Lee and J. S. J. Van Deventer, *Colloids Surf., A*, 2002, **211**, 115–126.
36 R. A. A. B. Santa, A. M. Bernardin, H. G. Riella and N. C. Kuhnen, *J. Cleaner Prod.*, 2013, **57**, 302–307.
37 A. G. San Cristóbal, R. Castelló, M. M. Luengo and C. Vizcayno, *Appl. Clay Sci.*, 2010, **49**, 239–246.
38 E. Álvarez-Ayuso, X. Querol, F. Plana, A. Alastuey, N. Moreno, M. Izquierdo, O. Font, T. Moreno, S. Diez, E. Vázquez and M. Barra, *J. Hazard. Mater.*, 2008, **154**, 175–183.
39 P. Chindaprasirt, C. Jaturapitakkul, W. Chalee and U. Rattanasa, *Waste Manage.*, 2009, **29**, 539–543.